

# Bottom-Up Fabrication of a Sandwich-Like Carbon/Graphene Heterostructure with Built-In FeNC Dopants as Non-Noble Electrocatalyst for Oxygen Reduction Reaction

Xiaoxia Lv,<sup>[a]</sup> Xue Xue,<sup>[a]</sup> Xingyu Gan,<sup>[a]</sup> Chenhao Lv,<sup>[a]</sup> Xiaochen Sun,<sup>[a]</sup> Yun Wang,<sup>[a]</sup> Liangjun Li,<sup>\*[b]</sup> and Hua Wang<sup>\*[a]</sup>

**Abstract:** High-performance non-noble electrocatalysts for oxygen reduction reaction (ORR) are the prerequisite for large-scale utilization of fuel cells. Herein, a type of sandwich-like non-noble electrocatalyst with highly dispersed FeN<sub>x</sub> active sites embedded in a hierarchically porous carbon/graphene heterostructure was fabricated using a bottom-up strategy. The in situ ion substitution of Fe<sup>3+</sup> in a nitrogen-containing MOF (ZIF-8) allows the Fe-heteroatoms to be uniformly distributed in the MOF precursor, and the assembly of Fe-doped ZIF-8 nano-crystals with graphene-oxide and in situ reduction of graphene-oxide afford a sandwich-like Fe-doped ZIF-8/graphene heterostructure. This type of heterostructure enables simultaneous optimization of FeN<sub>x</sub> active sites, architecture and interface properties for

obtaining an electron-catalyst after a one-step carbonization. The synergistic effect of these factors render the resulting catalysts with excellent ORR activities. The half-wave potential of 0.88 V vs. RHE outperforms most of the non-noble metal catalyst and is comparable with the commercial Pt/C (20 wt%) catalyst. Apart from the high activity, this catalyst exhibits excellent durability and good methanol-tolerance. Detailed investigations demonstrate that a moderate content of Fe dopants can effectively increase the intrinsic activities, and the hybridization of graphene can enhance the reaction kinetics of ORR. The strategy proposed in this work gives an inspiration towards developing efficient noble-metal-free electrocatalysts for ORR.

## Introduction

Oxygen-reduction reaction (ORR) is the cathode reaction of hydrogen-air fuel cells, a promising energy conversion device owing to its high energy efficiency and completely clean combustion emissions.<sup>[1]</sup> However, the conventional Pt-based ORR catalyst is notorious for its high-cost and vulnerable stability, which has largely impeded the wide spread utilization of fuel cells. In this context, the development of efficient non-noble catalysts for ORR has been the focus of many researchers around the world.<sup>[1b,2]</sup> Among several types of materials been reported, the MN<sub>x</sub> (M = Fe, Co, Ni et al., x = 2–4) doped carbon-based materials hold the greatest promise for practical applications due to their high activity and huge reserve.<sup>[3]</sup> It has been revealed that highly dispersing MN<sub>x</sub> sites embedded in carbon


matrix could render the resulting catalyst with high catalytic activity that rival conventional Pt-based catalysts.<sup>[4]</sup> Of those strategies been reported,<sup>[5]</sup> using metal-organic frameworks (MOFs) has been proved as an effective mean to immobilize highly dispersing MN<sub>x</sub> active sites in resulting carbonized materials because of their highly ordered structure and uniformly distributed metal struts.<sup>[5b,6]</sup> Furthermore, the big family of MOFs offers great flexibility in selecting the organic or inorganic components of MOFs, thus facilitating the finely tuning over structures and functionality in resulting catalysts.<sup>[7]</sup>

As an electro-catalyst, the optimal ORR catalyst not only need to lower down the reaction barrier to break O–O bond in adsorbed O<sub>2</sub> molecules, but also need to facilitate electron transfer, as well as mass transport of reactants and reaction products.<sup>[7b,8]</sup> Therefore, the strategy of developing efficient ORR catalyst should not just focused on local microstructure, that is, active sites, chemical compositions and defects etc., but also need an overall consideration at both of micro- and macroscopic level.<sup>[9]</sup> In this regard, the ideal ORR catalyst should be those materials with advanced architectures and multiply favorable factors.<sup>[10]</sup> While most of current studies are focusing on creating highly active catalytic sites, especially single-atomic MN<sub>x</sub> sites,<sup>[5b,11]</sup> the simultaneous optimization on pore structure, electronic structure and morphology in one material still remains rare.<sup>[12]</sup>

Graphene is an emerging materials attracting intensive attentions in many fields due to their unique electronic properties and ultrahigh electron conductivity.<sup>[13]</sup> Their intriguing properties also stimulated researchers to develop several gra-

[a] Dr. X. Lv, X. Xue, X. Gan, C. Lv, X. Sun, Y. Wang, Prof. H. Wang  
Institute of Medicine and Materials Applied Technologies  
College of Chemistry and Chemical Engineering  
Qufu Normal University  
Qufu City, Shandong Province 273165 (P. R. China)  
E-mail: huawang@qfnu.edu.cn

[b] Dr. L. Li  
Institute of New Energy  
College of New Energy  
China University of Petroleum (East China)  
Qingdao, Shandong Province 266580 (P. R. China)  
E-mail: lilj@upc.edu.cn

 Supporting information and the ORCID identification number(s) for the author(s) of this article can be found under:  
<https://doi.org/10.1002/asia.201901616>

phene-based hetero-structures and to explore their performance in energy related applications.<sup>[13,14]</sup> When assembled with MOFs, the graphene not only can exert a special electronic property, but also can offer a confining and stabilizing effect to components of MOFs.<sup>[15]</sup> This effect could prevent migration of active sites during the subsequent carbonization process.<sup>[4a]</sup> In this regard, the MOF/graphene heterostructure could be an ideal precursor that enable the multi-scale optimization over structures for resulting ORR catalysts.<sup>[16]</sup> Although some graphene-based hetero-structures have been reported previously,<sup>[15b,17]</sup> there is still an urgent need to develop such advanced ORR catalysts. And the detailed investigations of contributions of each factors are still needed to be elucidated. Herein, we report a bottom-up strategy to fabricate a type of carbon/graphene heterostructure with multi-scale optimization over active sites, pore structure and architecture. The obtained non-noble ORR catalysts (termed as FeNC/rGO) exhibit excellent performance that can rival the commercial Pt/C catalyst. Not only higher activity, the obtained ORR catalyst show superior durability and methanol tolerance to Pt/C catalyst. Furthermore, detailed investigations demonstrate that Fe-dopants and graphene hybridization play different roles in improving ORR performance.

## Results and Discussion

In order to construct this type of hetero-structure composite, the uniform dispersion of Fe dopants and the simultaneously assembly graphene-oxide with nano-sized MOFs is the key step. Therefore, a short-time solvothermal reaction that enables in situ doping and in situ assembly was employed in this work. The FeNC/rGO catalyst is synthesized through a procedure illustrated in Figure 1 a–1 c. Through an one-pot reaction of 2-methyl imidazole (MIM), Zn<sup>II</sup> salt, Fe<sup>III</sup> salt, graphene-oxide(GO) aqueous solution and polyvinyl pyrrolidone (PVP), the rGO-Fe-ZIF-8 heterostructure formed (see experimental details in Experimental section). During this procedure, substitution of Fe<sup>3+</sup> ions in framework of ZIF-8, the reduction of graphene-oxide, and the assembly of nano-sized MOF crystals with graphene take place simultaneously. It is well established that PVP can improve the interface compatibility between rGO and ZIF-8 particles.<sup>[18]</sup> Upon the addition of PVP, the ZIF-8 crystals could be encapsulated by rGO, leading to the rGO-Fe-ZIF-8 composite structure rather than the mixture of two separated phases.

The accordance between powder X-ray diffraction (PXRD) patterns of precursor with simulated pattern of ZIF-8 suggest that the MOF particle in rGO-Fe-ZIF-8 has the isomorphic structure with pristine ZIF-8 (as shown in Figure 1 d). The sharp peaks in PXRD patterns suggest that this MOF is of high degree of crystallinity. Scanning electron microscopy (SEM) images reveal a pure phase of truncated rhombic dodecahedra shape particles with a mean dimension of about 300 nm (as shown in Figure 2 a). These nano-sized MOF crystals are wrapped by graphene, as suggested by thin and curved films lying between crystal grains and on surface of crystals. TEM image also clearly displays thin graphene sheets lying outside and between these ZIF-8 particles (as shown in Figure 2 b). The EDS

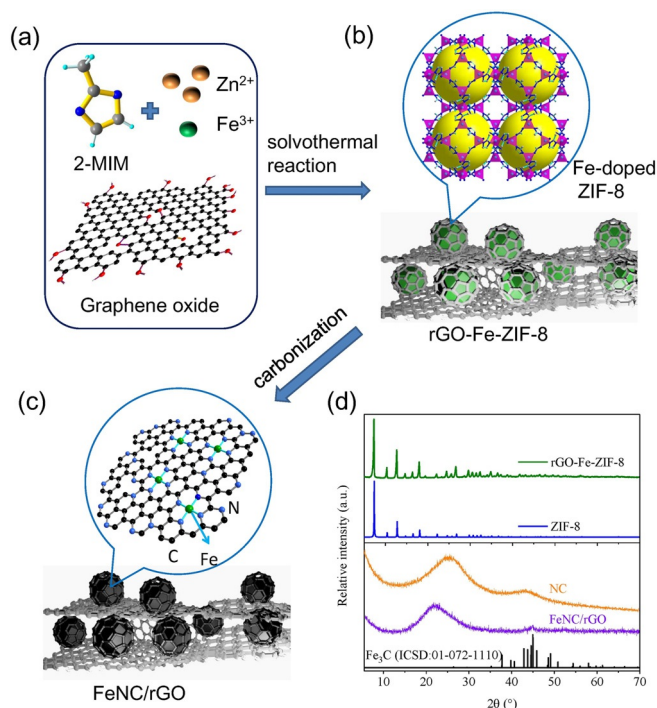


**Figure 1.** Schematic illustration of preparation process of FeNC/rGO: a) the metal ions, ligand and graphene oxide; b) the Fe-doped ZIF-8 (inset: the crystallographic structure of ZIF-8); c) the FeNC/rGO (inset: the structure of FeN<sub>x</sub>-doped carbons); d) PXRD patterns of the precursor rGO-Fe-ZIF-8 (up) and FeNC/rGO (down);

mapping analysis suggests that Fe-dopants could be uniformly distributed into both of MOF particles and rGO-sheets (Figure 2 c). This phenomenon might be rationalized by the fact that the rGO-Fe-ZIF-8 was prepared from an one-pot solvothermal reaction, in which the reactants of Fe<sup>III</sup> salt, Zn<sup>II</sup> salt, 2-MIM and PVP were mixed together prior to the subsequent solvothermal reaction. Also, oxygen could be uniformly distributed on both of the outer surface of crystals and the in-between crystals. The observation of O element could be assigned to the presence of rGO in those areas, since the surface of rGO prepared might contain large amounts of hydroxyl groups on its surface,<sup>[19]</sup> whereas ZIF-8 has no O-containing groups. X-ray photoelectron spectroscopy (XPS) of rGO-Fe-ZIF-8 suggests the co-existence of both Zn and Fe metal centers in this precursor (see XPS results in Figure S1 in supporting information). High-resolution Fe<sub>2p</sub> XPS spectrum reveals that the majority of Fe species are Fe<sup>2+</sup>, suggesting that most of Fe<sup>3+</sup> ions are reduced during the assembly process (see XPS results in Figure S2 in supporting information). Above results demonstrate that the Fe-hybridized ZIF-8 nano crystals are assembled with graphene in a well-organized heterostructure. It is worthy to note that these multiple characteristics evolved in this hetero-structure are simultaneously achieved through a facile one-pot reaction which would be important for practical utilizations.

After the carbonization of rGO-Fe-ZIF-8 precursor at 1000 °C under Ar atmosphere, the sandwich-like FeN<sub>x</sub> doped carbon/rGO heterostructure were obtained (termed as FeNC/rGO). PXRD patterns for FeNC/rGO catalysts displays two broad

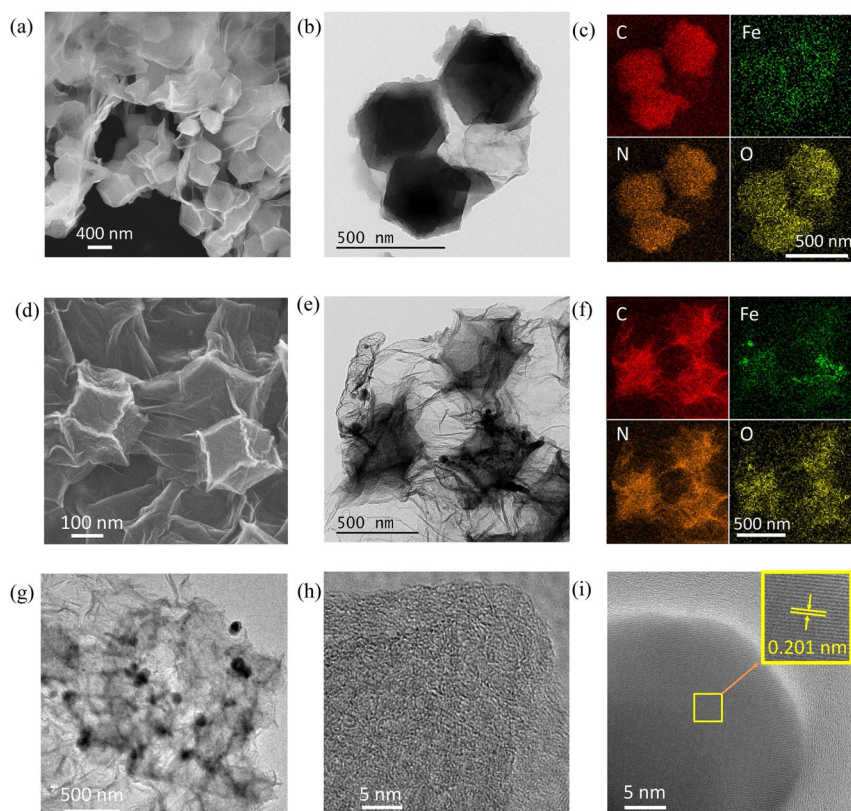


**Figure 2.** a) SEM image of rGO-Fe-ZIF-8; b) TEM image of rGO-Fe-ZIF-8; c) EDS elemental mapping of rGO-Fe-ZIF-8; d) SEM image of FeNC/rGO; e) TEM image of FeNC/rGO; f) EDS elemental mapping of FeNC/rGO; g) HRTEM image of FeNC/rGO; h) HRTEM image of FeNC/rGO showing the disordered carbon; i) HRTEM image of FeNC/rGO showing the lattice fringe of Fe containing species (inset: the magnified lattice fringe of Fe-containing species).

peaks at  $24^\circ$  and  $44^\circ$ , which can be ascribed to the (002) and (101) planes of graphite carbon sheets (see Figure 1 d). The minor peaks at  $42.6^\circ$  and  $44.5^\circ$  on PXRD patterns correspond to the nano-sized  $\text{Fe}_3\text{C}$  which is of low degree of crystallinity.<sup>[19]</sup> SEM images shows that the FeNC/rGO catalysts inherits the morphology of precursors, except of slightly reduced particle size from 300 nm to 200 nm (as shown in Figure 2 d). Thin curved films observed both on the surface of polyhedral particles and inter-nanoparticles are graphene sheets. TEM images (Figure 2 e) confirm the co-existence of both nano-sized metal-containing particles and thin graphene sheets. Nano-sized polyhedron-shaped particles are embedded in thin graphene sheets to form a flocculent texture. This configuration is a well-organized structure which not only facilitate the oxygen diffusion, but also can increase electron conductivity.

The EDS elemental mapping analysis reveals that nano-sized Fe-containing particles could exist in this composite material with a broad background (Figure 2 f), indicating that highly dispersing  $\text{Fe}_x$  sites might be comprised in the carbon matrix. A considerable amount of oxygen-containing groups are also found in those areas with an overlay of rGO sheets. High-resolution TEM images (HRTEM) (Figure 2g) suggests that the carbon matrix is composed of carbon sheets and nano-sized Fe-containing particles. As shown in Figure 2h, the carbon is highly disordered and these carbon sheets are staggered with each other. The HRTEM (Figure 2i) also displays clear lattice

fringes with a lattice spacing of 0.201 nm. This lattice spacing could be ascribed to the (220) plane of the  $\text{Fe}_3\text{C}$ , which is agreeable with PXRD patterns.

$\text{N}_2$  adsorption isotherms were performed at 77 K to evaluate the porosity of FeNC/rGO (as shown in Figure 3 a). The typical type- isotherm suggest a hierarchical pore structure for FeNC/rGO. The BET surface areas for this series of catalyst is in the range of  $582\text{--}992\text{ m}^2\text{ g}^{-1}$ , which decreases with the increasing content of Fe (as shown in Figure S3 in supporting information). The lower surface area found in high Fe-containing samples can be attributed to the higher degree of crystallization induced by Fe species. At a same Fe content, the BET surface area shows a no-significant variation with the content of graphene. Pore size distribution (PSD) derived from non-local density function theory (NLDFT) based on  $\text{N}_2$  isotherm confirmed the hierarchical pore structure for these FeNC/rGO. For FeNC/rGO<sub>0.015</sub>, *meso*-pores centered at 6 nm micro-pore centered at 1.2 nm can be observed on PSD curves. Compared to the N-doped carbon (NC) which derived from the direct carbonization of ZIF-8, the introduction of rGO and Fe-dopants significantly increase the ratio of *meso*-pores in resulting catalyst. A larger pore volume and higher content of *meso*-pores can be observed when increasing the content of graphene. The higher porosity can be ascribed to the increased pore space caused by the inter-crossed graphene sheets. As the higher porosity and higher content of *meso*-pores can provide greater

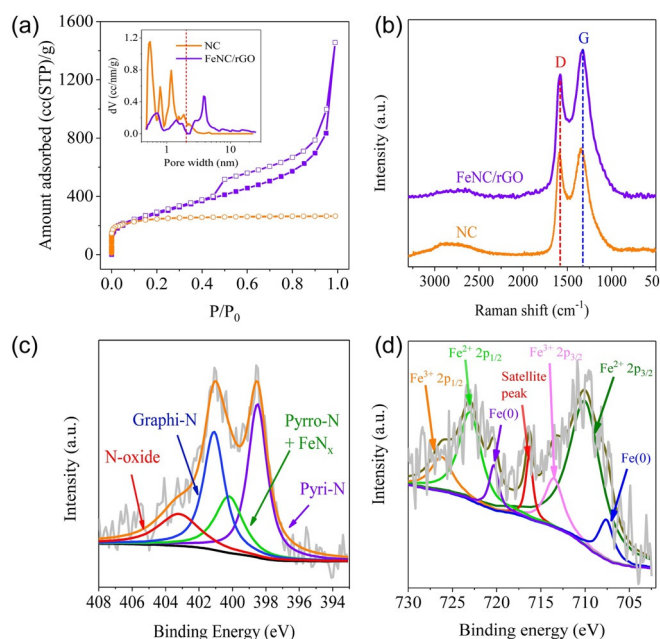


**Figure 3.** a) Pore size distributions derived from  $\text{N}_2$  isotherm of FeNC/rGO (inset); b) Raman spectrum of FeNC/rGO; c) High resolution XPS spectra of  $\text{N}_{1s}$ ; d) High resolution XPS spectrum of  $\text{Fe}_{2p}$ .

accessibility to reactants, they are vital in improving ORR properties.<sup>[4a]</sup>

To investigate the local fine structure of carbon matrix and metal containing species, Raman spectrum and XPS spectra were measured for FeNC/rGO. As shown in Figure 3b, Raman spectrum reveals both characteristics of ordered graphite ( $1576 \text{ cm}^{-1}$ ) and amorphous carbon ( $1325 \text{ cm}^{-1}$ ). Compared to the NC, the higher  $I_g/I_d$  value in FeNC/rGO can be ascribed to the contribution of graphene. XPS survey for FeNC/rGO unveils the presence of Fe, N, C and O elements in FeNC/rGO. As shown in Figure 3c, high-resolution XPS spectra for  $\text{N}_{1s}$  reveal four forms of N groups: pyridinic-N ( $398.5 \text{ eV}$ ), pyrrolic-N ( $400.2 \text{ eV}$ ), graphitic-N ( $401.1 \text{ eV}$ ) and N-oxide ( $403.2 \text{ eV}$ ).<sup>[3a,20]</sup> Because of the binding energy of pyridinic-N is very similar to  $\text{FeN}_x$  group, the high content of pyridinic-N should comprise of the contribution of  $\text{FeN}_x$  group.<sup>[21]</sup> The deconvoluted high resolution XPS spectrum of  $\text{Fe}_{2p}$  is shown in Figure 3d. The peaks at  $710$  and  $723 \text{ eV}$  can be ascribed to the  $2p_{3/2}$  and  $2p_{1/2}$  peaks of  $\text{Fe}^{2+}$ . And the peaks at  $713.5$  and  $726.2 \text{ eV}$  can be assigned to the  $2p_{3/2}$  and  $2p_{1/2}$  peaks of  $\text{Fe}^{3+}$ , respectively. The satellite peak at  $716.3 \text{ eV}$  suggests that both  $\text{Fe}^{2+}$  and  $\text{Fe}^{3+}$  are co-existed in this catalyst. A small amount of  $\text{Fe}^0$  (peaks at  $707.6$  and  $720.3 \text{ eV}$ ) can be observed, suggesting that some of Fe species might have been reduced to metallic Fe during the carbonization process. Notably, the peak near  $710 \text{ eV}$  can also be assigned to the contribution of  $\text{FeN}_x$  which are considered to be highly efficient active sites for ORR.<sup>[21]</sup> The content of Fe were determined by Inductive Coupled Plasma Emission Spectrometer (ICP). The contents of Fe heteroatoms are in the range of  $0.82$  to  $7.71\%$  which can be tuned by adjusting the Fe/Zn ratio in reactants (as shown in Table S1 in supporting information). Elemental analysis revealed that N content in this

series of catalyst is in the range of  $3.28$ – $8.76\%$ . The N content varied with the different content of Fe heteroatoms.

This type of well-organized hetero-structure motivate us to investigate their ORR properties. The comparison of ORR performance for these catalysts can be evaluated from linear sweep voltammogram (LSV) profiles as shown in Figure 4a. Compared to N-doped carbon (NC) which contains no Fe species, the FeNC derived from Fe-doped ZIF-8 exhibit much more positive on-set potential ( $E_{\text{on-set}}$ ) and half-wave potential ( $E_{1/2}$ ), suggesting that the introduction of Fe species can significantly improve ORR activity. Furthermore, the introduction of graphene on FeNC give rise to the FeNC/rGO which exhibit a much improved ORR activity over FeNC. In order to verify the role of ZIF-8, the FeN-PC which was derived from the Fe salts and rGO was also prepared, without adding ZIF-8. As shown in Figure 4a, much lower  $E_{1/2}$  of FeN-PC ( $0.795 \text{ V}$  vs. RHE) was obtained as compared to FeNC/rGO, indicating that the hybridization of ZIF-8 in precursor could significantly enhance the reaction kinetics of ORR for resulting catalyst. On the FeNC/rGO with an optimized structure and composition, the  $E_{\text{on-set}}$  of FeNC/rGO reaches  $0.968 \text{ V}$  vs. RHE, and the limited current density is closed to  $6 \text{ mA cm}^{-2}$ . The corresponding  $E_{1/2}$  is  $0.88 \text{ V}$

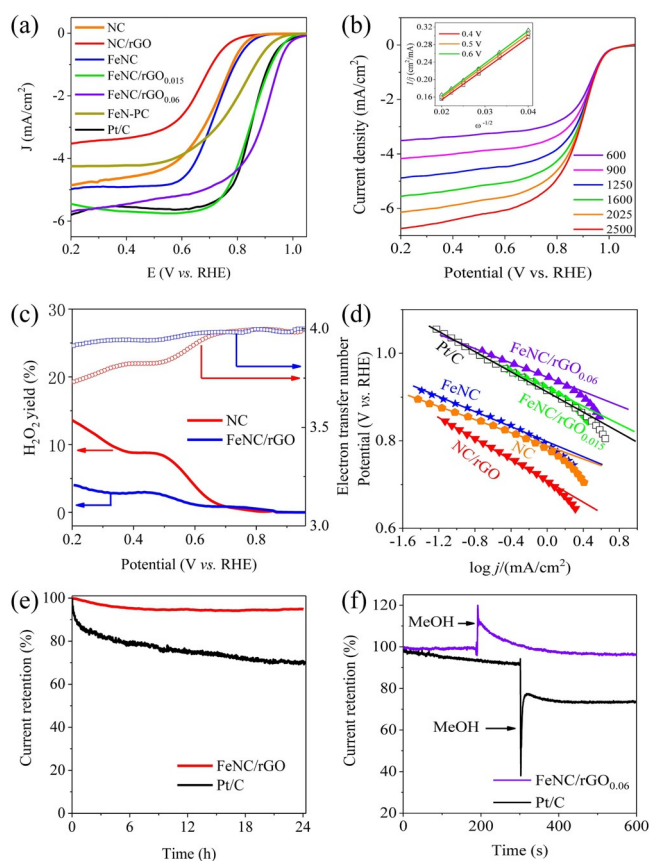


**Figure 4.** a) LSV curves of NC, NC/rGO, FeNC, FeNC/rGO and Pt/C catalysts at a rotating speed of  $1600 \text{ rpm}$  in  $\text{O}_2$ -saturated KOH electrolyte (scanning rate:  $5 \text{ mV sec}^{-1}$ ); b) LSV profiles at variable rotating speeds and the electron transfer numbers (inset); c) yield rate of  $\text{H}_2\text{O}_2$  and electron transfer number; d) Tafel slopes of different catalysts; e) Comparison of stability of FeNC/rGO and Pt/C catalyst; f)  $I$ - $t$  curves for FeNC/rGO and Pt/C catalyst with the addition of Methanol ( $2 \text{ M}$ ).

vs. RHE. Based on these values, we can conclude that the ORR activity of FeNC/rGO is comparable with that of commercial Pt/C (20 wt%) catalyst. Noteworthy, these values are also in the top ranks of catalytic activity among non-noble catalysts towards ORR.<sup>[6b,22]</sup> In the acid medium (0.5 M H<sub>2</sub>SO<sub>4</sub>), this catalyst also exhibited a considerably high ORR activity, with an E<sub>on-set</sub> of 0.86 V vs. RHE and an E<sub>1/2</sub> of 0.72 V vs. RHE (seeing the LSV profiles in Figure S4 in Supporting information). This activity could be ascribed to the contribution of Fe<sub>Nx</sub> active sites highly dispersed in the carbon matrix.

Based on the LSV profiles at different rotating speed, an electron transfer number of 3.90 can be derived from the Koutecky-Levich (K-L) method for FeNC/rGO<sub>0.06</sub> at 0.5 V vs. RHE (as shown in Figure 4b). This value suggests that the oxygen reduction process on FeNC/rGO undergoes a four-electron pathway which is considered as the most efficient reaction pathway for ORR. To further validate the reaction pathways for ORR, rotating ring-disk electrode (RRDE) measurements were performed on FeNC/rGO<sub>0.06</sub> (as shown in Figure 4c). The electron transfer number determined from RRDE measurements is 3.85, which suggests a four-electron pathway of ORR process on FeNC/rGO. In accordance with this four-electron process, low yields of H<sub>2</sub>O<sub>2</sub> (2–6%) is produced on this series of catalysts. Ultra-low yields of H<sub>2</sub>O<sub>2</sub> confirms that four-electron pathway dominates the ORR process on FeNC/rGO. Furthermore, lower Tafel slopes of 80.3 mV dec<sup>-1</sup> for FeNC/rGO<sub>0.06</sub> compared with Pt/C indicate the fast reaction kinetics of ORR (as shown in Figure 4d).

Besides activity, durability is also a crucial factor that should be considered in practical applications. As shown in Figure 4e, the FeNC/rGO retain 97.5% of its original current density after 12 hours of running in alkaline medium, compared with 65% of retention for commercial Pt/C catalyst under the same test conditions. The superior durability of FeNC/rGO can be partially ascribed to the favorable chemical structure of active sites. Furthermore, the graphene could also provide a protection effect which prevents the leaching of active sites. As a non-noble catalyst, FeNC/rGO showed an outstanding methanol tolerance (as shown in Figure 4f). After addition of methanol, there is no clear decay in current density for FeNC/rGO. In contrast, the current density dropped significantly after addition of methanol for Pt/C catalyst, suggesting the poisoning of Pt/C catalyst.

To elucidate the contributions of structural parameters to ORR activity, the ORR performance on a series of FeNC/rGO were investigated, using Fe content and graphene dosage as the entry. E<sub>on-set</sub> and E<sub>1/2</sub>, which can be regarded as indicative of over-potential and reaction kinetics, respectively, are correlated with two structural parameters. As shown in Figure 5a, it is clear that the introduction of Fe active sites can significantly improve the E<sub>on-set</sub>. However, with the further increasing Fe contents in FeNC/rGO, the values of E<sub>on-set</sub> remains similar. This phenomenon demonstrates that the over-potential of ORR is determined by the intrinsic properties of active sites, rather than the numbers of active sites. Different from E<sub>on-set</sub>, the Fe content has a large impact on E<sub>1/2</sub>. It is shown that the plot of E<sub>1/2</sub> vs. Fe content shows a volcano-shaped curve, suggesting that the moderate Fe content exhibits the most positive E<sub>1/2</sub> values. This phenomenon demonstrates that the moderate content of Fe can render the resulting catalyst with the highest ORR activity, which is in accordance with the results from other reports.<sup>[23]</sup> From the structural aspect, the moderate Fe content enables the Fe-containing active sites to be distributed in the carbon matrix in a highly dispersing form, leading to the largest number of accessible active sites. In contrast, the high Fe content would result in the aggregation of active sites, which inversely decreases the number of accessible active sites. Other than Fe active sites, the introduction of graphene also shows a positive impact on ORR performance. As shown in Figure 5b, the FeNC/rGO exhibit a much superior E<sub>1/2</sub> compared to that without graphene. The general positive relationship between E<sub>1/2</sub> and graphene dosage demonstrates the positive effect of graphene on ORR kinetics. It is well known that the addition of graphene can improve the electron transfer rate, which is beneficial to lower down the reaction barrier and accelerate the reaction kinetics. Furthermore, from a perspective of catalyst design, the hybridization of graphene in catalyst is beneficial to ORR due to its function in promoting the dispersion of catalyst and facilitating the diffusion of reactants and products.

Based on above results, we can conclude that the introduction of FeNC active sites and hybridization of graphene in catalyst plays different roles in improving ORR performance. These two structural parameters can function synergistically given that they are introduced into catalyst in an optimized structure. Therefore, the architecture proposed in this work may

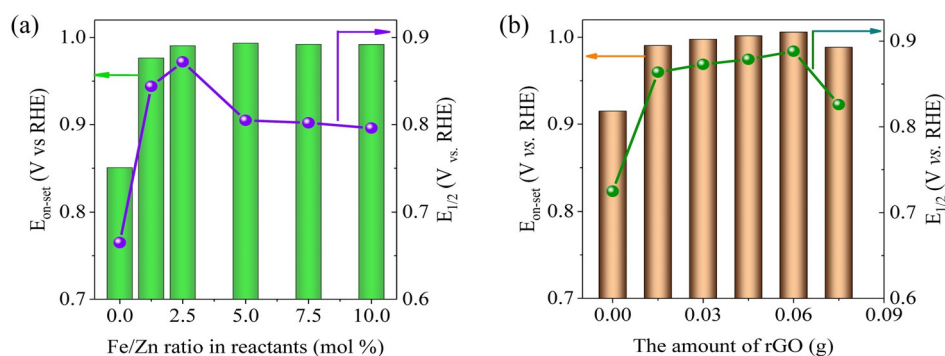


Figure 5. a) Comparison of E<sub>on-set</sub> and E<sub>1/2</sub> at different Fe contents in FeNC/rGO; b) Comparison of E<sub>on-set</sub> and E<sub>1/2</sub> at different content of rGO in FeNC/rGO.

provide a good solution to fabricate effective non-noble ORR catalyst.

## Conclusions

In summary, a type of non-noble ORR catalyst which consists of  $\text{FeN}_x$  active sites and sandwich-like carbon/graphene heterostructure was fabricated. The in situ doping of Fe into the framework of ZIF-8 under solvothermal conditions combined with the in situ assembly of graphene-oxide with ZIF-8 crystals and reduction of graphene-oxide afford a sandwich-like hierarchically composite. Through a one-step carbonization of precursor, a type of sandwich-like carbon/graphene heterostructure which consists of highly dispersed  $\text{FeN}_x$  active sites and interconnected graphene was obtained. This type of catalyst exhibits excellent ORR activities that is comparable with that of commercial Pt/C catalyst. Comparison studies reveal that the  $\text{FeN}_x$  active sites and graphene can function synergistically to boost ORR performance. Furthermore, this type of non-noble catalyst exhibits a durability and methanol tolerance superior to that of commercial Pt/C catalyst. The outstanding ORR performance of this type of catalyst confirms the effectiveness of this strategy in promoting ORR activities, and it may also inspire further development of advanced catalysts for other energy-related applications.

## Experimental Section

### Chemicals and apparatus

All of the starting materials including 2-methyl imidazole (2-MIM),  $\text{Zn}(\text{NO}_3)_2 \cdot 6\text{H}_2\text{O}$ ,  $\text{Fe}(\text{NO}_3)_3 \cdot 9\text{H}_2\text{O}$ , N, N-dimethyl formamide (DMF) are purchased from J&K Scientific, LTD and are used without further purifications. Nalfon solution is purchased from Dupont. Commercial Pt/C catalysts (20 wt%) used as reference catalyst was purchased from Johnson Matthey. The graphene-oxide (0.3 wt%) were prepared through a Hummers method according to the reported procedure.<sup>[15a,24]</sup>

Powder X-ray diffraction patterns were measured on a Panalytical X'Pert diffractometer ( $\text{Cu}_{K\alpha}$ ,  $\lambda = 0.15418 \text{ nm}$ ). Scanning electron microscopy (SEM) were collected by a Hitachi E-1010 Cold Field scanning electron microscope. Transition electron microscopic images were collected on a JEM2100F transmission electron microscopy. High resolution TEM (HRTEM) images were collected on a FEI Tecnai G2 F20 field emission transmission electron microscope. Raman spectrum were collected by Lab Raman HR Evolution spectrometer at a laser wavelength of 633 nm. X-ray photoelectron spectrum (XPS) were measured on a ULVAC-PHI Quantum 2000 ( $\text{Al}_{K\alpha}$ ). Elemental analysis (EA) of C, H and N were performed on a German Elementary Vairo El Cube instrument. Inductive Coupled Plasma (ICP) were measured on a Varian 720-OES ICP apparatus.  $\text{N}_2$  adsorption isotherms at 77 K were performed on a Quantachrome Autosorb BET analyzer. Non-local density functional theory (NLDFT) was employed to calculate the pore size distribution.

### Preparation procedure of $\text{rGO}_x\text{-Fe}_y\text{-ZIF-8}$ (x refers to the amount of graphene, and y refer to the ratio of Fe/Zn)

As a typical procedure, 3.35 g  $\text{Zn}(\text{NO}_3)_2 \cdot 6\text{H}_2\text{O}$  and y g  $\text{Fe}(\text{NO}_3)_3 \cdot 9\text{H}_2\text{O}$  (y equals to x multiply the molar quantity of  $\text{Zn}(\text{NO}_3)_2 \cdot 6\text{H}_2\text{O}$  and

then multiply the molar weight of  $\text{Fe}(\text{NO}_3)_3 \cdot 9\text{H}_2\text{O}$ ) were dissolved in 100 mL methanol. 0.25 g of PVP was added into above solution and was stirred until dissolved. In another bottle, 2-MIM (3.695 g) was added into 100 mL methanol and was stirred until dissolved. The methanol solution of 2-MIM was poured into the solution of metal ions and was subjected to a rigorous stirring for 3 minutes. After that, a certain amount of GO aqueous solution was added into above mixtures and was then stirred for 5 minutes. The obtained mixture was treated by ultrasonic for 5 minutes and heated at 120 °C for 120 minutes in an oven. After cooling to ambient temperature, the product was separated through centrifugation. The obtained products was washed with methanol for at least three times to remove the unreacted ligands or metal ions and then washed with water for one time. Then, the obtained product was dried through a freeze-drying process.

### Preparation procedure of FeNC/rGO

The FeNC/rGO was prepared from the direction carbonization of  $\text{rGO-Fe}_x\text{-ZIF-8}$  in a tube furnace in Ar atmosphere. As a general procedure, the precursor of  $\text{rGO-Fe}_x\text{-ZIF-8}$  (1.0 g) was placed in a 5 mL corundum boat which was then placed in the middle of the tube furnace. After replacing the air with flowing Ar gas, the furnace was heated to 1000 °C at a heating speed of 5 °C  $\text{min}^{-1}$  and maintained at corresponding temperature for 2 hours, and then furnace was cooled naturally to ambient temperature. The obtained catalyst was washed with diluted hydrochloric acid (6 M) and dried at 100 °C for 2 hours.

### Preparation procedure of NC

The nitrogen-doped carbon (NC) is prepared from the direct carbonization of ZIF-8 which contains no Fe dopants. The ZIF-8 is prepared through the following method:  $\text{Zn}(\text{NO}_3)_2 \cdot 6\text{H}_2\text{O}$  (3.35 g) and 2-MIM (3.695 g) were dissolved in 100 mL methanol separately. Then, the solution of a  $\text{Zn}(\text{NO}_3)_2$  and 2-MIM were mixed together and was stirred for 24 hours at room temperatures. The product was separated through centrifugation and was washed with methanol for three times. The obtained product was dried in 60 °C for 2 hours. After a same carbonization process as FeNC/rGO, a nitrogen-doped carbon (termed as NC) was obtained.

### Preparation procedure of NC/rGO

The preparation procedure of NC/rGO was similar to that of FeNC/rGO except that no  $\text{Fe}(\text{NO}_3)_3 \cdot 9\text{H}_2\text{O}$  was added into the solution of  $\text{Zn}(\text{NO}_3)_2 \cdot 6\text{H}_2\text{O}$ . After a same carbonization process as FeNC/rGO, a nitrogen-doped carbon/rGO composite material (termed as NC/rGO) was obtained.

### Preparation procedure of FeN-PC

The preparation procedure of FeN-PC is similar as that of FeNC/rGO, except for no ligand and  $\text{Zn}^{II}$  salt added in the reactant mixtures. In order to reduce the GO solution to rGO, a slightly exceeding amount of hydrazine hydrate (50%) was added into the above mixture. After the subsequent solvothermal reaction, filtration, washing and a freeze-drying, the obtained powder was subjected to the heat treatment at 1000 °C for 2 h under Ar atmosphere. After cooling to room temperature, the FeN-doped porous carbon (termed as FeN-PC) was obtained

### Electrochemical measurements:

The ORR measurements were performed on a CHI-760e electrochemical workstation. Before measurements, catalyst ink was prepared by dispersing 4 mg catalyst into 1800  $\mu\text{L}$  of ethanol/ $\text{H}_2\text{O}$  (1/1, v/v) solution. 200  $\mu\text{L}$  Nafion solution was added into above solution, and the resulting mixture was subjected to sonication for 15 minutes to ensure the complete dispersion of catalyst. The working electrode was prepared by depositing 5  $\mu\text{L}$  of catalyst ink on the glass-carbon electrode (3 mm) and was dried at 60  $^\circ\text{C}$  for 15 minutes.

The ORR activity of all samples were measured on a three-electrode system equipped with a rotating disk electrode (RDE). The KOH aqueous solution (0.1 M) was used as the electrolyte. The Ag/AgCl and Pt electrode were used as the reference electrode and counter electrode, respectively. The potential versus Ag/AgCl was converted to the potential versus RHE through a following equation [Eq. (1)]:

$$E(\text{RHE}) = E(\text{Ag}/\text{AgCl}) + 0.965 \quad (1)$$

Linear sweep voltammogram (LSV) was measured in  $\text{O}_2$ -saturated KOH solution (0.1 M) at a rotating speed of 1600 rpm and a sweeping rate of  $-5 \text{ mV s}^{-1}$ . The electron transfer number was calculated using the Koutecky-Levich (K-L) equation [Eqs. (2)-(4)] based on the LSV profiles at different rotating speed.

$$\frac{1}{j} = \frac{1}{j_L} + \frac{1}{j_K} = \frac{1}{B\omega^{1/2}} + \frac{1}{j_K} \quad (2)$$

$$B = 0.62 n F C_0 (D_0)^{2/3} \nu^{-1/6} \quad (3)$$

$$j_K = n F k C_0 \quad (4)$$

The rotating ring-disk electrode (RRDE) was employed to measure the  $\text{H}_2\text{O}_2$  yield and electron transfer number. The procedure of measurements was similar with RDE measurements except that the ring-disk electrode was used in replace of the disk electrode. And the  $\text{H}_2\text{O}_2$  yield and electron transfer number were calculated through the following equations [Eqs. (5)-(6)].

$$n = \frac{4I_D}{I_D + \frac{I_R}{N}} \quad (5)$$

$$y_{\text{H}_2\text{O}_2} = 100 \frac{2I_R/N}{I_D + I_R/N} \quad (6)$$

in which  $n$  and  $y_{\text{H}_2\text{O}_2}$  represent the electron transfer number and  $\text{H}_2\text{O}_2$  yield, respectively;  $I_D$  and  $I_R$  are the disk current and ring current, respectively;  $N$  is the electron collection efficiency which is calibrated through a reference experiment using Potassium Ferricyanide solution as the electrolyte (the measured value is 0.36 in this work).

### Acknowledgements

We are grateful for the financial support from the National Natural Science Foundation of China (nos. 21601106 and 21675099), the Higher Educational Science and Technology Program of Shandong Province, China (Grant No. J15LC04), the Major Basic Research Program of Natural Science Foundation of Shandong Province, P. R. China (ZR2018ZC0129), the Key Re-

search and Development Plan of Shandong Province (2018GGX104108) and the Fundamental Research Funds for the Central Universities (18CX02068A).

### Conflict of interest

The authors declare no conflict of interest.

**Keywords:** FeNC catalyst • graphene • metal-organic frameworks • non-noble catalyst • oxygen reduction reaction

- [1] a) M. K. Debe, *Nature* **2012**, *486*, 43–51; b) T. Ioroi, Z. Siroma, S.-i. Yamazaki, K. Yasuda, *Adv. Energy Mater.* **2019**, *9*, 1801284.
- [2] a) Z. W. Seh, J. Kibsgaard, C. F. Dickens, I. Chorkendorff, J. K. Nørskov, T. F. Jaramillo, *Science* **2017**, *355*, eaad4998; b) D. S. Su, G. Sun, *Angew. Chem. Int. Ed.* **2011**, *50*, 11570–11572; *Angew. Chem.* **2011**, *123*, 11774–11777.
- [3] a) W.-J. Jiang, L. Gu, L. Li, Y. Zhang, X. Zhang, L.-J. Zhang, J.-Q. Wang, J.-S. Hu, Z. Wei, L.-J. Wan, *J. Am. Chem. Soc.* **2016**, *138*, 3570–3578; b) M. Lefèvre, E. Proietti, F. Jaouen, J.-P. Dodelet, *Science* **2009**, *324*, 71–74.
- [4] a) H. T. Chung, D. A. Cullen, D. Higgins, B. T. Sneed, E. F. Holby, K. L. More, P. Zelenay, *Science* **2017**, *357*, 479–484; b) W. Liu, L. Zhang, X. Liu, X. Liu, X. Yang, S. Miao, W. Wang, A. Wang, T. Zhang, *J. Am. Chem. Soc.* **2017**, *139*, 10790–10798.
- [5] a) B.-C. Hu, Z.-Y. Wu, S.-Q. Chu, H.-W. Zhu, H.-W. Liang, J. Zhang, S.-H. Yu, *Energy Environ. Sci.* **2018**, *11*, 2208–2215; b) H. Zhang, S. Hwang, M. Wang, Z. Feng, S. Karakalos, L. Luo, Z. Qiao, X. Xie, C. Wang, D. Su, Y. Shao, G. Wu, *J. Am. Chem. Soc.* **2017**, *139*, 14143–14149.
- [6] a) L. Jiao, G. Wan, R. Zhang, H. Zhou, S. H. Yu, H. L. Jiang, *Angew. Chem. Int. Ed.* **2018**, *57*, 8525–8529; *Angew. Chem.* **2018**, *130*, 8661–8665; b) L. Li, J. He, Y. Wang, X. Lv, X. Gu, P. Dai, D. Liu, X. Zhao, *J. Mater. Chem. A* **2019**, *7*, 1964–1988; c) N. Cheng, L. Ren, X. Xu, Y. Du, X. Dou Shi, *Adv. Energy Mater.* **2018**, *8*, 1801257.
- [7] a) A. Indra, T. Song, U. Paik, *Adv. Mater.* **2018**, *30*, 1705146; b) L. Li, P. Dai, X. Gu, Y. Wang, L. Yan, X. Zhao, *J. Mater. Chem. A* **2017**, *5*, 789–795.
- [8] A. Kulkarni, S. Siahrostami, A. Patel, J. K. Nørskov, *Chem. Rev.* **2018**, *118*, 2302–2312.
- [9] a) W. Xia, R. Zou, L. An, D. Xia, S. Guo, *Energy Environ. Sci.* **2015**, *8*, 568–576; b) H. Hu, L. Han, M. Yu, Z. Wang, X. W. Lou, *Energy Environ. Sci.* **2016**, *9*, 107–111.
- [10] B. Y. Guan, Y. Lu, Y. Wang, M. Wu, X. W. Lou, *Adv. Funct. Mater.* **2018**, *28*, 1706738.
- [11] a) J. Wang, Z. Huang, W. Liu, C. Chang, H. Tang, Z. Li, W. Chen, C. Jia, T. Yao, S. Wei, Y. Wu, Y. Li, *J. Am. Chem. Soc.* **2017**, *139*, 17281–17284; b) F. Li, G.-F. Han, H.-J. Noh, S.-J. Kim, Y. Lu, H. Y. Jeong, Z. Fu, J.-B. Baek, *Energy Environ. Sci.* **2018**, *11*, 2263–2269.
- [12] M. Luo, Y. Yang, S. Guo, *Chem* **2019**, *5*, 260–262.
- [13] M. Liu, R. Zhang, W. Chen, *Chem. Rev.* **2014**, *114*, 5117–5160.
- [14] a) Z. Fan, J. Yan, L. Zhi, Q. Zhang, T. Wei, J. Feng, M. Zhang, W. Qian, F. Wei, *Adv. Mater.* **2010**, *22*, 3723–3728; b) Y. Yan, Y.-X. Yin, Y.-G. Guo, L.-J. Wan, *Adv. Energy Mater.* **2014**, *4*, 1301584; c) W. Xia, C. Qu, Z. Liang, B. Zhao, S. Dai, B. Qiu, Y. Jiao, Q. Zhang, X. Huang, W. Guo, D. Dang, R. Zou, D. Xia, Q. Xu, M. Liu, *Nano Lett.* **2017**, *17*, 2788–2795.
- [15] a) M. Jiang, L. Li, D. Zhu, H. Zhang, X. Zhao, *J. Mater. Chem. A* **2014**, *2*, 5323–5329; b) Z. Li, C. Li, X. Ge, J. Ma, Z. Zhang, Q. Li, C. Wang, L. Yin, *Nano Energy* **2016**, *23*, 15–26.
- [16] J. Liu, Q. Ma, Z. Huang, G. Liu, H. Zhang, *Adv. Mater.* **2018**, *30*, 1800696.
- [17] H. X. Zhong, J. Wang, Y. W. Zhang, W. L. Xu, W. Xing, D. Xu, Y. F. Zhang, X. B. Zhang, *Angew. Chem. Int. Ed.* **2014**, *53*, 14235–14239; *Angew. Chem.* **2014**, *126*, 14459–14463.
- [18] Z. Liang, C. Zhang, H. Yuan, W. Zhang, H. Zheng, R. Cao, *Chem. Commun.* **2018**, *54*, 7519–7522.
- [19] a) M.-Q. Wang, C. Ye, M. Wang, T.-H. Li, Y.-N. Yu, S.-J. Bao, *Energy Storage Mater.* **2018**, *11*, 112–117; b) W. Yang, X. Liu, X. Yue, J. Jia, S. Guo, *J. Am. Chem. Soc.* **2015**, *137*, 1436–1439.
- [20] A. Mahmood, H. Tabassum, R. Zhao, W. Guo, W. Aftab, Z. Liang, Z. Sun, R. Zou, *Small* **2018**, *14*, 1803500.

- [21] X. Liu, H. Liu, C. Chen, L. Zou, Y. Li, Q. Zhang, B. Yang, Z. Zou, H. Yang, *Nano Res.* **2019**, *12*, 1651–1657.
- [22] X. Wang, Z. Li, Y. Qu, T. Yuan, W. Wang, Y. Wu, Y. Li, *Chem* **2019**, *5*, 1486–1511.
- [23] a) S. H. Ahn, X. Yu, A. Manthiram, *Adv. Mater.* **2017**, *29*, 1606534; b) A. Zitolo, V. Goellner, V. Armel, M.-T. Sougrati, T. Mineva, L. Stievano, E. Fonda, F. Jaouen, *Nat. Mater.* **2015**, *14*, 937–942.
- [24] S. Guo, S. Dong, *Chem. Soc. Rev.* **2011**, *40*, 2644–2672.

---

Manuscript received: November 22, 2019  
 Revised manuscript received: December 27, 2019  
 Version of record online: January 20, 2020

---